Ferroelastic-switching-driven large shear strain and piezoelectricity in a hybrid ferroelectric

Hu, Yuzhong; You, Lu; Xu, Bin; Li, Tao; Morris, Samuel Alexander; Li, Yongxin; Zhang, Yehui; Wang, Xin; Lee, Pooi See; Fan, Hong Jin; Wang, Junling

2021

Hu, Y., You, L., Xu, B., Li, T., Morris, S. A., Li, Y., ... Wang, J. (2021). Ferroelastic-switching-driven large shear strain and piezoelectricity in a hybrid ferroelectric. Nature Materials. doi:10.1038/s41563-020-00875-3

https://hdl.handle.net/10356/146195

https://doi.org/10.1038/s41563-020-00875-3

Ferroelastic-switching-driven large shear strain and piezoelectricity in a hybrid ferroelectric

Yuzhong Hu[1,2,†], Lu You[3,†], Bin Xu[3,†], Tao Li[2], Samuel Alexander Morris[5], Yongxin Li[6], Yehui Zhang[3], Xin Wang[3], Pooi See Lee[2], Hong Jin Fan[1,*] and Junling Wang[2,4,*]

[1]School of Physical and Mathematical Sciences, Nanyang Technological University, Singapore 637371

[2]School of Materials Science and Engineering, Nanyang Technological University, Singapore 639798

[3]Jiangsu Key Laboratory of Thin Films, School of Physical Science and Technology, Soochow University, 1 Shizi Street, Suzhou 215006, China

[4]Department of Physics, Southern University of Science and Technology, Shenzhen 518055, China

[5]Facility for Analysis, Characterisation, Testing and Simulation (FACTS), Nanyang Technological University, Singapore, 639798

[6]Division of Chemistry and Biological Chemistry, School of Physical and Mathematical Sciences, Nanyang Technological University, Singapore 637371

†These authors contributed equally to this work.

*Corresponding author. Email: jwang@sustech.edu.cn (J.W.); fanhj@ntu.edu.sg (H.J.F.)

Keyword: hybrid ferroelectric, shear strain, ferroelastic switching, piezoelectric, crystal structure confinement

Materials that can produce large controllable strains are widely used in shape memory devices, actuators and sensors[1, 2], and great efforts have been made to improve strain outputs[3-6]. Among them, ferroelastic transitions underpin giant reversible strains in electrically-driven ferro/piezoelectrics and thermally- or magnetically-driven shape memory alloys[7, 8]. However, large-strain ferroelastic switching in conventional ferroelectrics is very challenging while magnetic and thermal controls are not desirable for applications. Here, we demonstrate a large shear strain of up to 21.5 % in a hybrid ferroelectric, $C_6H_5N(CH_3)_3CdCl_3$, two orders of magnitude higher than conventional ferroelectric polymers and oxides. It is achieved by inorganic bond switching and facilitated by structural confinement of the large organic moieties, which prevents undesired 180° polarization switching. Furthermore, Br substitution can soften the bonds, enabling a sizable shear piezoelectric coefficient (d_{35} ~ 4830 pm/V) at the Br-rich end of the solid solution, $C_6H_5N(CH_3)_3CdBr_{3x}Cl_{3(1-x)}$. The electromechanical properties of these compounds suggest their potential in lightweight and high energy density devices, and the strategy described here could inspire the development of next generation piezoelectrics and electroactive materials based on hybrid ferroelectrics.

The archetype of shape memory alloys, NiTi, can produce a strain of 6-8 % from a temperature induced reversible phase transition[9]. Other shape memory alloys can be triggered by magnetic fields. NiMnGa, for instance, shows up to 10 % shear strain due to twin boundary movements under a magnetic field[10]. Perovskite piezoelectric oxides can achieve strains above 0.1 % at morphotropic phase boundaries[11]. Through point-defect engineering and/or ferroelastic domain switching, ferroelectric single crystals show strains up to 0.75 % in aged $BaTiO_3$[5], while a maximum strain up to 1.7 % was recorded in lead-based relaxors[3]. For polymer systems, various stimuli have been explored to generate strains, including change in pH, temperature, light, moisture, magnetic and electric fields[12]. Due to their

structural flexibility, the strain response of some polymers, e.g., elastomers, can even surpass 100 %[4].

However, although many materials are available for various applications, very few satisfy the requirements of large strain, high energy density and high speed simultaneously. For example, shape memory alloys can produce large stress and medium strain, but the actuation output is always at a low speed[13]. Piezoelectric oxides can generate large stress at high speed, but the strain response is much lower than that of other materials. Polymers, on the contrary, produces the largest strain but one to two orders of magnitude lower actuation stress (2 MPa on average)[13]. Organic-inorganic hybrid ferroelectrics (OIHF) comprise of inorganic frameworks filled with organic moieties. It is thus possible that they can take advantages of both the lightweight, flexible organic moiety and the mechanically strong and tough inorganic backbone, producing large strain with high energy/power output[14, 15]. In recent years, various OIHFs have been designed and investigated, particularly, making great progress towards piezoelectric and electrostrictive applications[16-18]. Piezoelectric responses of some OIHFs have even outperformed traditional oxide ferroelectrics such as $BaTiO_3$ and Pb(Zr, Ti)O_3 (PZT) [18, 19]. The multiaxial nature of these OIHFs implies that ferroelastic switching may lie at the core of the enhanced piezoelectricity[20]. However, direct proof of deterministic control of ferroelastic switching is still lacking.

The ferroelectricity in most OIHFs originates from the off-center ordering of the positively charged organic moieties, which link with the inorganic frameworks through hydrogen bond and van der Waals interaction. The reversal of the spontaneous polarization sometimes requires a complete flip of the large organic moiety, in stark contrast to oxide ferroelectrics, where polarization switching only involves relatively small displacement of the ions. It is thus possible to suppress the strain-equivalent 180° polarization switching in OIHFs with large molecular moiety due to the high energy barrier and promote ferroelastic

switching with large strain response. Following this strategy, we synthesize and investigate a hybrid ferroelectric, $C_6H_5N(CH_3)_3CdCl_3$ ((PTMA)$CdCl_3$), which produces colossal ferroelastic shear strain about two orders of magnitude higher than that of lead-based piezoelectrics and larger than all shape memory alloys hitherto reported. The non-volatile, reversible strain is attributed to macroscopic ferroelastic switching reflecting atomic-level lattice distortions, thanks to the structural confinement effect. Furthermore, we demonstrate that Br substitution effectively softens the bonds and flattens the switching energy landscape, leading to large shear piezoelectric response at Br-rich ends of the solid solution (PTMA)$CdBr_{3x}Cl_{3(1-x)}$.

X-ray diffraction (XRD) and differential scanning calorimetry (DSC) measurements were carried out to investigate the crystal structures and phase transitions of (PTMA)$CdBr_{3x}Cl_{3(1-x)}$. Going from Cl to Br, the lattice constants of the compounds increase continuously (**Table 1 and Supplementary Fig. S1**), while phase transition temperature keeps decreasing from above 180 °C (decomposition temperature) to 19 °C (**Supplementary Fig. S2**). However, no structural transition is induced by Br substitution. Powder XRD refinements indicate that the solid solutions all crystallize in monoclinic *Cc* space group in the low temperature phase (LTP) and orthorhombic *Ama2* in the high temperature phase (HTP) (**Table 1 and Supplementary Table 1**), which can be described by the Aizu notation of *mm2*F*m* among the 88 ferroelectric transition species[21]. In the LTP, (PTMA)$CdBr_{3x}Cl_{3(1-x)}$ consists of PTMA organic moieties and a scaffold of 1D edge-sharing cadmium-halide (CdX_5^-) hexahedra (see **Fig. 1a** and **Supplementary Fig. S3 & S4** for pure Cl, Br and mixed halide structures, respectively). They are connected via hydrogen bonds between the methyl group and the halide anions. In the HTP, the longest Cd-X bond of the hexahedron breaks, transforming into corner-sharing CdX_4^- tetrahedron. In the meantime, order-disorder phase transition is triggered in the organic part with two degenerate positions and the restoration of

mirror symmetry with respect to the (001) plane (**Supplementary Text 1**).

The ferroelectric polarization of (PTMA)$CdBr_{3x}Cl_{3(1-x)}$ in the LTP can be understood by regarding N and Cd sites as the centers of positive and negative charges in the unit cell, respectively. As shown in **Fig. 1c**, the spontaneous polarization has components along both the ***a*** and ***c*** axes, as confirmed by in-plane piezoresponse force microscopy (PFM) (**Supplementary Fig. S5**), and is in accordance with the monoclinic symmetry. However, due to the large size of the organic moiety and confined space between the inorganic chains, a 180° reversal of the polarization is energetically unlikely. This is evidenced by the fact that the polarization along the ***a*** axis persists even in the HTP. Fortunately, polarization switching along the ***c*** axis is not hindered by the structure, which will rotate the polarization vector and generate large shear strain as shown in **Fig. 1c**. Experimentally, polarization-electric field (*P*-*E*) hysteresis loops can only be obtained along the ***c*** axis, while no polarization switching is observed along the ***a*** axis prior to electrical breakdown. The unique polarization switching path is consistent with the *mm2*F*m* Aizu notion, suggesting that symmetry breaking across the phase transition occurs only along one axis, as evidenced by the dielectric anomaly (**Supplementary Fig. S6**). Remarkably, upon polarization switching, the macroscopic tilting angle of the (PTMA)$CdCl_3$ crystal exhibits an appreciable change (~ 12.8 °) that perfectly correlates with the unit cell distortion ($\Delta\beta = 12.6\,°$) (**Fig. 1c, also see Supplementary Movies S1 and S2**), which translates to a shear strain $S\,(= \tan\Delta\beta)$ of ~ 22 %.

Quantitative polarization and shear strain measurements were performed on the solid solutions by simultaneously recording the *P*-*E* and strain-electric field (*S*-*E*) hysteresis loops using the setup shown in **Fig. 1b** (see Methods for details). Note that the measurements were conducted at elevated temperatures to facilitate the polarization switching (**Supplementary Fig. S7**), as commonly practiced for hybrid ferroelectrics[18, 19]. As shown in **Fig. 2a**, with increasing Br content, the remanent polarization (P_r) decreases monotonically from 3.6

μC/cm^2 to 3.0 μC/cm^2, which agrees well with the calculated polarizations of 3.7 μC/cm^2 for the pure Cl compound and 2.9 μC/cm^2 for the Br counterpart (**Supplementary Text 2**). Additionally, Br substitution apparently reduces the energy barrier for polarization switching, as indicated by the reduction of the critical temperature for switching and the coercive field. Shear strain (S) in this case is defined as $S = \tan\Delta\beta \cong d/H$, where d is the shear strain induced movement of the upper surface, H is the height of sample and $\Delta\beta$ is the shear angle (**Supplementary Text 3**)[22]. As shown in **Fig. 2b**, the reversible shear strain hits a record-breaking value of ~ 21.5 % for the pure Cl compound, and decreases with increasing Br content, which agrees with the smaller β angle in Br-rich compounds (**Table 1**). Given that the shear modulus C_{55} of (PTMA)$CdCl_3$ is about 5.8 GPa based on our first principles calculations (**Supplementary Text 2**), we estimate a stress output of 40 MPa and a volumetric energy density of 4.2 MJ/m^3. In **Fig. 2c**, we compare reported actuation strain and volumetric energy density for various material systems (see details in **Supplementary Table 2**). The maximum shear strain of (PTMA)$CdCl_3$ is about two orders of magnitude higher than those of conventional ferroelectrics, surpassing all the reported shape memory alloys. Note that most electroactive polymers (EAPs) produce strains based on Maxwell stress, and the electric field needed are in the order of MV/cm, much larger than the field used here[23]. And for temperature-driven shape memory alloys (TSMAs) and shape memory polymers (SMPs), the response time is very long compared to our material (**Supplementary Movie S3**)[2]. So, the appropriate comparison should be with ferroelectric oxides (FE oxides), piezoelectric polymers and magnetically-driven shape memory alloys (MSMAs), and (PTMA)$CdCl_3$ performs better than all of them.

More intriguingly, with Br substitution, the lattice is softened significantly and large shear piezoelectric response is achieved in Br-rich compounds. Unipolar piezoelectric response was measured on the solid solution series that have been *pre-poled* using the same

experimental setup as shown in **Fig. 1b**. Following Voigt notation, the piezoelectric coefficient measured in our setup is d_{35}[24], which can be calculated by $d_{35} = S_5/E_3$, namely, the slope of the *S* – *E* curves. Owing to the nonlinearity and hysteresis of the curve, the so-called "large-signal" piezoelectric coefficient d_{35}^* approximates to S_{max}/E_{max} [11, 25] (**Supplementary Text 3**). As shown in Fig. 3a, d_{35}^* increases monotonically with more Br substitution and reaches a maximum value of around 4830 pm/V for 90% Br compound at low frequency (2 Hz) and under large field (6 kV/cm). The shear piezoelectric coefficient is higher than recently discovered organic[26], hybrid piezoelectrics[18], as well as other classical oxide piezoelectrics (**Fig. 3d**)[27], and comparable to those of top performing single-crystal relaxors[28]. The greatly enhanced piezoelectric response in Br-rich crystals is attributed to the chemical-substitution induced bond softening. This not only increases the *intrinsic* piezoelectricity of the compound, but also enhances the *extrinsic* contribution of ferroelastic domain wall motion (switching) to the electromechanical response[29, 30]. This is evidenced by the obvious field and frequency dependence of the piezoelectric behavior observed in 90% Br sample (**Fig. 3b, c**), which correlates with the Rayleigh-like behavior of the dielectric response (**Supplementary Fig. S9, S10**)[31]. By examining the maximum strain in **Fig. 2b** and the monoclinic angle in **Table 1**, we can find that pure Cl sample was poled into an almost single-domain state, while Br-rich samples were not. Under large field (along the same direction as the pre-poling field) at low frequency, the back-switched ferroelastic domains are activated again and contribute to the observed piezoelectric response. However, the involvement of ferroelastic switching inevitably leads to hysteresis effect, which could be alleviated via targeted chemical engineering to achieve relaxor-like properties[32, 33]. The unique electromechanical behavior of our OIHF is highlighted by a direct comparison with the classic oxide ferroelectric relaxor, $Pb(Mg_{1/3}Nb_{2/3})O$-$0.3PbTiO_3$ (PMN-PT) single crystal (**Fig. 3e, f and Supplementary Fig. S8**). The asymmetric bipolar *S*-*E* curve reflects the

ferroelastic switching induced shear strain, enabled by the suppression of 180° polarization switching in our sample. As for the unipolar piezoelectric response, even though the d_{35}^{*} of the 90% Br compound is not larger than that of the PMN-PT, but the maximum attainable strain is. This is likely due to the high elasticity of the OIHF that makes the sample more resistant to brittle facture.

To better understand the effect of Br substitution, we carried out *ab initio* density functional theory (DFT) calculations for (PTMA)$CdCl_3$ and (PTMA)$CdBr_3$. **Figure 4a** shows the minimum energy paths for switching between the two ferroelastic states, illustrating that the energy barrier in Br compound is greatly reduced with more flattened double-well landscape compared to the Cl counterpart. It is worth to note that the intermediate state of the ferroelastic switching is featured by mirror-symmetric corner-sharing CdX_4^- tetrahedra in which the longest Cd-X bond is broken, a reminiscence of the HTP structure. The switching process can be visualized as the bond switching (breaking and reformation) between Cd and the two adjacent apex halide atoms (**Supplementary Movies S4 and S5**). We then evaluated the bond strength by calculating the crystal orbital Hamilton populations (COHPs) of the longest Cd-X bond, as well as the two shortest hydrogen bonds (X-H1 and X-H2) for comparison (**Fig. 4b**). Indeed, as characterized by the integrated COHPs up to the Fermi energy (**Fig. 4b and Supplementary Table 4**), stronger Cd-X and X-H bonds are found in the Cl compound, which is consistent with the higher electronegativity of Cl than Br, and the Cd-X bond is expected to have a dominant contribution to the overall barrier. Last, the piezoelectric response of the compounds under large electric field was calculated. The results reproduce the ferroelastic switching events and verify that the large piezoelectricity originates from the extrinsic effect of ferroelastic domain wall motion, instead of the intrinsic linear lattice deformation (**Supplementary Figure S11**)[30].

Our study reveals the great potential of hybrid ferroelectrics in achieving large electromechanical responses. The strategy of structural confinement combined with the diversity of organic molecules make it possible to tailor electromechanical outputs by tactical consideration of the size, symmetry and conformation of the molecules.

References

1. Trolier-McKinstry, S. & Muralt, P. Thin Film Piezoelectrics for MEMS. *J. Electroceramics* **12**, 7-17 (2004).
2. Mohd Jani, J., Leary, M., Subic, A. & Gibson, M.A. A review of shape memory alloy research, applications and opportunities. *Mater. Des. (1980-2015)* **56**, 1078-1113 (2014).
3. Park, S.-E. & Shrout, T.R. Ultrahigh strain and piezoelectric behavior in relaxor based ferroelectric single crystals. *J. Appl. Phys.* **82**, 1804-1811 (1997).
4. Pelrine, R., Kornbluh, R., Pei, Q. & Joseph, J. High-Speed Electrically Actuated Elastomers with Strain Greater Than 100%. *Science* **287**, 836-839 (2000).
5. Ren, X. Large electric-field-induced strain in ferroelectric crystals by point-defect-mediated reversible domain switching. *Nat. Mater.* **3**, 91-94 (2004).
6. Lai, A., Du, Z., Gan, C.L. & Schuh, C.A. Shape memory and superelastic ceramics at small scales. *Science* **341**, 1505-1508 (2013).
7. Chopra, H.D., Ji, C. & Kokorin, V.V. Magnetic-field-induced twin boundary motion in magnetic shape-memory alloys. *Phys. Rev. B* **61**, R14913-R14915 (2000).
8. Nagarajan, V. *et al.* Dynamics of ferroelastic domains in ferroelectric thin films. *Nat. Mater.* **2**, 43-47 (2003).
9. Otsuka, K. & Ren, X. Physical metallurgy of Ti–Ni-based shape memory alloys. *Prog. Mater. Sci.* **50**, 511-678 (2005).
10. Chmielus, M., Zhang, X.X., Witherspoon, C., Dunand, D.C. & Müllner, P. Giant magnetic-field-induced strains in polycrystalline Ni–Mn–Ga foams. *Nat. Mater.* **8**, 863-866 (2009).
11. Hao, J., Li, W., Zhai, J. & Chen, H. Progress in high-strain perovskite piezoelectric ceramics. *Mater. Sci. Eng. R Rep.* **135**, 1-57 (2019).
12. Meng, H. & Hu, J. A Brief Review of Stimulus-active Polymers Responsive to Thermal, Light, Magnetic, Electric, and Water/Solvent Stimuli. *J. Intell. Mater. Syst. Struct.* **21**, 859-885 (2010).
13. Huber, J.E., Fleck, N.A. & Ashby, M.F. The selection of mechanical actuators based on performance indices. *Proc. R. Soc. Lond. A* **453**, 2185-2205 (1997).
14. Mitzi, D.B. Templating and structural engineering in organic–inorganic perovskites. *J. Chem. Soc., Dalton Trans.*, 1-12 (2001).
15. Li, W. *et al.* Chemically diverse and multifunctional hybrid organic–inorganic perovskites. *Nat. Rev. Mater.* **2**, 16099 (2017).
16. Chen, B. *et al.* Large electrostrictive response in lead halide perovskites. *Nat. Mater.* **17**, 1020-1026 (2018).
17. Shu, L. *et al.* Photoflexoelectric effect in halide perovskites. *Nat. Mater.* **19**, 605-609 (2020).
18. Liao, W.-Q. *et al.* A molecular perovskite solid solution with piezoelectricity stronger than lead zirconate titanate. *Science* **363**, 1206-1210 (2019).
19. You, Y.-M. *et al.* An organic-inorganic perovskite ferroelectric with large piezoelectric response. *Science* **357**, 306-309 (2017).
20. Tang, Y.-Y. *et al.* Multiaxial Molecular Ferroelectric Thin Films Bring Light to Practical Applications. *J. Am. Chem. Soc.* **140**, 8051-8059 (2018).

21. Aizu, K. Possible Species of "Ferroelastic" Crystals and of Simultaneously Ferroelectric and Ferroelastic Crystals. *J. Phys. Soc. Jpn.* **27**, 387-396 (1969).
22. Malakooti, M.H. & Sodano, H.A. Direct measurement of piezoelectric shear coefficient. *J. Appl. Phys.* **113**, 214106 (2013).
23. Brochu, P. & Pei, Q. Dielectric Elastomers for Actuators and Artificial Muscles, in *Electroactivity in Polymeric Materials*. (ed. L. Rasmussen) 1-56 (Springer US, Boston, MA; 2012).
24. Altammar, H., Dhingra, A. & Salowitz, N. Ultrasonic Sensing and Actuation in Laminate Structures Using Bondline-Embedded d_{35} Piezoelectric Sensors. *Sensors* **18** (2018).
25. Viehland, D. *et al.* Effect of uniaxial stress on the large-signal electromechanical properties of electrostrictive and piezoelectric lead magnesium niobate lead titanate ceramics. *J. Appl. Phys.* **95**, 1969-1972 (2004).
26. Guerin, S. *et al.* Control of piezoelectricity in amino acids by supramolecular packing. *Nat. Mater.* **17**, 180-186 (2018).
27. Tressler, J.F., Alkoy, S. & Newnham, R.E. Piezoelectric Sensors and Sensor Materials. *J. Electroceramics* **2**, 257-272 (1998).
28. Li, F., Zhang, S., Xu, Z., Wei, X. & Shrout, T.R. Critical Property in Relaxor-$PbTiO_3$ Single Crystals – Shear Piezoelectric Response. *Adv. Funct. Mater.* **21**, 2118-2128 (2011).
29. Damjanovic, D. Stress and frequency dependence of the direct piezoelectric effect in ferroelectric ceramics. *J. Appl. Phys.* **82**, 1788-1797 (1997).
30. Bellaiche, L. & Vanderbilt, D. Intrinsic Piezoelectric Response in Perovskite Alloys: PMN-PT versus PZT. *Phys. Rev. Lett.* **83**, 1347-1350 (1999).
31. Damjanovic, D. & Demartin, M. The Rayleigh law in piezoelectric ceramics. *J. Phys. D: Appl. Phys.* **29**, 2057-2060 (1996).
32. Li, F. *et al.* Ultrahigh piezoelectricity in ferroelectric ceramics by design. *Nat. Mater.* **17**, 349-354 (2018).
33. Li, F. *et al.* Giant piezoelectricity of Sm-doped $Pb(Mg_{1/3}Nb_{2/3})O_3$-$PbTiO_3$ single crystals. *Science* **364**, 264-268 (2019).

Acknowledgements

We would like to acknowledge the Facility for Analysis, Characterisation, Testing and Simulation (FACTS) at Nanyang Technological University, Singapore for the use of XRD facilities, X. R. Zhou (School of Materials Science and Engineering, Nanyang Technological University) for the help in piezoelectric measurements, and F. Li (Xi'an Jiaotong University) for the discussion on piezoelectric resonance measurements. L.Y. and B.X. acknowledge the startup funds from Soochow University, and the support from Priority Academic Program Development (PAPD) of Jiangsu Higher Education Institutions. L.Y. also acknowledges the support from the National Natural Science Foundation of China (11774249, 12074278), the Natural Science Foundation of Jiangsu Province (BK20171209), and the Key University Science Research Project of Jiangsu Province (18KJA140004, 20KJA140001). H.J.F.

acknowledges the support from AME Individual Research Grant (Grant number: A1883c0004), Agency for Science, Technology, and Research (A*STAR). J.W. acknowledges the support from the Ministry of Education, Singapore (Grant numbers: AcRF Tier 1 118/17 and 189/18) and the startup grant from Southern University of Science and Technology (SUSTech), China.

Author contributions

Y.H., L.Y., H.J.F. and J.W. conceived the idea and designed the project. Y.H. grew the single crystals and performed the powder XRD measurements. S.A.M. and Y.H. conducted powder XRD analysis. Y.L. and S.A.M. performed the single crystal XRD characterization and analysis. Y.H. prepared the devices and carried out the PFM, ferroelectric, piezoelectric, dielectric, TGA and DSC measurements, and analyzed the results with L.Y., J.W. and H.J.F.. Y.H., T.L. and P.S.L. conducted shear strain characterizations. B.X., Y.Z., and X.W. carried out the DFT calculations. Y.H., L.Y., H.J.F. and J.W. wrote the manuscript with inputs from all authors.

Additional information

Supplementary information is available in the online version of the paper. Reprints and permissions information is available at www.nature.com/reprints. Correspondence and requests for materials should be addressed to J.W. or H.J.F.

Competing interests

The authors declare no competing interests.

Methods

Synthesis of (PTMA)$CdBr_{3x}Cl_{3(1-x)}$ ($0 \leq x \leq 1$) single crystal

All chemicals were purchased from Sigma-Aldrich and used as received. Single crystals of (PTMA)$CdBr_{3x}Cl_{3(1-x)}$ were synthesized by slow evaporation of filtered acetonitrile and deionized water mixture solutions (acetonitrile : deionized water=3:2 for 0≤ Br concentration ≤63%, 4:1 for 63%< Br concentration ≤100%) with stoichiometric ratios of PTMA-Cl, PTMA-Br, $CdCl_2$ and $CdBr_2 \cdot 4H_2O$. Hexagonal prism shape crystals with centimeter length were obtained upon slow evaporation of the solutions at room temperature for around three weeks. Pure bromide crystal is pale blue. With higher Cl amount, the color of the crystal becomes lighter. (PTMA)$CdBr_{3x}Cl_{3(1-x)}$ with Br percentage of 15%. 29%, 45%, 63%, 70%, 77%, 80% and 90% were obtained using precursors with Br molar percentage of 20%, 33%, 50%, 67%, 73%, 80%, 87% and 96%, respectively. Br concentration in the crystals were calculated based on the C, H, and N mass fraction measured by an elemental analyzer (PerkinElmer model 2400 Series II).

X-ray diffraction measurement

Powder X-ray diffraction (XRD) patterns were measured by using Cu Kα radiation (λ=1.540598 Å, 40 kV and 30 mA) on a commercial diffractometer (Panalytical Xpert). Single crystal XRD patterns were collected using a Bruker APEX II diffractometer with Mo source (λ=0.71073 Å). Crystal structures were solved using the Bruker SHELXTL Software Package and refined for all data by Full-matrix least-squares on F^2. All non-hydrogen atoms were subjected to anisotropic refinement. The hydrogen atoms were generated geometrically and allowed to ride in their respective parent atoms; they were assigned with appropriate isotropic thermal parameters and included in the structure factor calculations. The data can be

obtained free of charge from the Cambridge Crystallography Data Center via www.ccdc.cam.ac.uk/data_request/cif

Differential scanning calorimetry and thermogravimetric analyses measurements

Thermal analyses were performed using differential scanning calorimetry (DSC, TA INSTRUMENTS - Q10) by heating and cooling the single crystal samples a a rate of 5 K min^{-1} in an aluminum pan under nitrogen flow of atmospheric pressure. Thermogravimetric analyses (TGA, TA INSTRUMENTS – Q500) of the single crystals were measured at a rate of 10 K min^{-1} in air.

Dielectric and ferroelectric measurements

Temperature dependent measurements were performed on a cryogenic micromanipulator probe station equipped with a heating stage. Crystals were carefully cut in the form of plates along *a*, *b* and *c* crystallographic axes, respectively. Silver paste was coated on the top and bottom surfaces of the crystals as electrodes. Dielectric measurements were carried out using a commercial LCR meter (Agilent E4980A) with 1 V AC driving voltage. Ferroelectric properties were measured using a commercial ferroelectric tester (Precision LC, Radiant technologies) equipped with high-voltage amplifier (Precision 4kV HVI, Radiant technologies).

Piezoresponse force microscopy (PFM) measurement

PFM was conducted on a commercial atomic force microscope (Asylum Research MFP-3D) using soft Au-coated silicon tips with a spring constant of ~0.2 N m^{-1} (Budget Sensor, ContGB-G), to avoid sample surface damage. Resonance-enhanced dual AC resonance tracking (DART) mode (tip driven voltage=500mV, frequency ~220kHz) was used to enhance the signal-to-noise ratio[34].

Shear strain and piezoelectricity measurements

The measurement setup is shown in **Fig. 1b**. Crystals were firmly fixed on glass slide by epoxy and double side tape with ***bc*** (100) plane as the basal plane. Bar crystals (***c*** axis is the long axis) were carefully cleaved along (001) plane, which was then polished and covered with silver pastes as electrodes. An aluminum plate was attached on top of the crystal as the reflective mirror with its plane perpendicular to the top surface of the crystal and the laser beam. Electric field induced movement of top surface (shear strain) was measured by a commercial photonic sensor (MTI-2100 Fotonic). All samples were pre-poled for unipolar piezoelectric measurements. Shear strain (S) is calculated by $S = \tan\Delta\beta \cong d/H$, where d is the displacement recorded by the photonic sensor, H is the height of the sample and $\Delta\beta$ is the shear angle. d_{35} is calculated by $d_{35} = S_5/E_3$, where E_3 is the electric field applied along the ***c*** axis.

Computational methods

(PTMA)$CdCl_3$ and (PTMA)$CdBr_3$ crystals were simulated with four formula units by density functional theory (DFT). The calculations were carried out using the projected augmented wave (PAW) method[35] and the Perdew-Burke-Ernzerhof (PBE) exchange-correlation functionals[36], as implemented in the Vienna ab-initio simulation package (VASP)[37]. The energy cutoff for the plane wave expansion was set to 500 eV, and a 2×2×4 Monkhorst-Pack k-mesh is used. We explicitly treated 12 valence electrons for Cd ($4d^{10}5s^2$), 4 for C ($2s^22p^2$), 5 for N ($2s^22p^3$), 1 for H ($1s^1$), 7 for Cl ($3s^23p^5$) and 7 for Br ($4s^24p^5$). The initial structures were obtained from the experimental crystallographic data, then fully optimized until all atomic forces were less than 0.002 eV/Å. The effects of van der Waals (vdW) interactions[38] were included during the structural and electronic relaxations, as well as all the subsequent calculations. The ferroelectric polarizations were calculated by the Berry phase approach[39, 40],

and the elastic constants were determined from the strain-stress relationship. The minimum energy paths for polarization switching were calculated using the generalized solid-state nudged elastic band (GSSNEB) method[41]. We used the LOBSTER package to compute the crystal orbital hamiltonian populations (COHP)[42-44], with a 3×3×5 Monkhorst-Pack k-mesh.

Data availability

The data that support the findings of this study are available within the article and its Supplementary Information or on figshare.com, DOI: 10.6084/m9.figshare.13227434.

Supplementary References

34. Rodriguez, B.J., Callahan, C., Kalinin, S.V. & Proksch, R. Dual-frequency resonance-tracking atomic force microscopy. *Nanotechnology* **18**, 475504 (2007).
35. Blöchl, P.E. Projector augmented-wave method. *Phys. Rev. B* **50**, 17953-17979 (1994).
36. Perdew, J.P., Burke, K. & Ernzerhof, M. Generalized Gradient Approximation Made Simple. *Phys. Rev. Lett.* **77**, 3865-3868 (1996).
37. Kresse, G. & Joubert, D. From ultrasoft pseudopotentials to the projector augmented-wave method. *Phys. Rev. B* **59**, 1758-1775 (1999).
38. Grimme, S. Semiempirical GGA-type density functional constructed with a long-range dispersion correction. *J. Comput. Chem.* **27**, 1787-1799 (2006).
39. Resta, R. Macroscopic polarization in crystalline dielectrics: the geometric phase approach. *Rev. Mod. Phys.* **66**, 899-915 (1994).
40. King-Smith, R.D. & Vanderbilt, D. Theory of polarization of crystalline solids. *Phys. Rev. B* **47**, 1651-1654 (1993).
41. Sheppard, D., Xiao, P., Chemelewski, W., Johnson, D.D. & Henkelman, G. A generalized solid-state nudged elastic band method. *J. Phys. Chem. Lett* **136**, 074103 (2012).
42. Dronskowski, R. & Bloechl, P.E. Crystal orbital Hamilton populations (COHP): energy-resolved visualization of chemical bonding in solids based on density-functional calculations. *J. Phys. Chems.* **97**, 8617-8624 (1993).
43. Deringer, V.L., Tchougréeff, A.L. & Dronskowski, R. Crystal Orbital Hamilton Population (COHP) Analysis As Projected from Plane-Wave Basis Sets. *J. Phys. Chems. A* **115**, 5461-5466 (2011).
44. Maintz, S., Deringer, V.L., Tchougréeff, A.L. & Dronskowski, R. LOBSTER: A tool to extract chemical bonding from plane-wave based DFT. *J. Comput. Chem.* **37**, 1030-1035 (2016).

Table 1| Structural information of (PTMA)$CdBr_{3x}Cl_{3(1-x)}$ in the LTP.

Br amount (%)	0	15	29	45	63	70	77	80	90
a / Å	12.7541	12.8262	12.8497	12.8960	12.9338	12.9763	12.9909	13.0015	13.0465
b / Å	14.5035	14.5961	14.6257	14.6785	14.7126	14.7458	14.7443	14.7601	14.7827
c / Å	7.1515	7.2275	7.2554	7.31681	7.3650	7.4153	7.4261	7.4567	7.5058
β / °	96.3069	95.910	95.823	95.5064	95.282	94.985	95.035	95.000	94.841
Vol / Å³	1314.86	1345.89	1356.50	1378.63	1395.54	1413.54	1416.92	1425.52	1442.43
Space Group	*Cc*	*Cc*	*Cc*	*Cc*	*Cc*	*Cc*	*Cc*	*Cc*	*Cc*

Figure captions

Fig. 1 | Crystal structures and photos of (PTMA)$CdCl_3$ in two different ferroelastic states. a, Perspective of crystallographic structure along the 1D chain (*c*) direction. **b**, Experimental setup for the shear strain and piezoelectricity measurements. Silver paste is applied on the *ab* planes of the crystal as electrodes, and the electric field is applied along the 1D chain (*c*) direction. The numbers in the coordinate denote the Voigt notation of the strain tensor. **c**, Upper panel: Illustration of structural units in the two ferroelastic states and structure confinement effect for ferroelectric/ferroelastic switching. Yellow and green arrows indicate polarization directions. Lower panel: Photos of a bulk single crystal poled to the two ferroelastic states by electric field, showing a macroscopic shear strain in good correlation with the unit cell distortion.

Fig. 2 | Ferroelectric and ferroelastic properties of (PTMA)$CdBr_{3x}Cl_{3(1-x)}$. a, *P-E* loops and **b**, shear *S-E* loops of the solid solution series at a measurement frequency of 2 Hz. **c**, Actuation strain and work outputs for various material systems, i.e., ferroelectric (FE) oxides, piezoelectric polymer, magnetic-driven shape memory alloys (MSMAs), temperature-driven shape memory alloys (TSMAs), electroactive polymers (EAPs), shape memory polymers (SMPs) and hybrid FE (see **Supplementary Table 2** for detailed data and references).

Fig. 3 | Large-signal piezoelectric properties of (PTMA)$CdBr_{3x}Cl_{3(1-x)}$. a, Unipolar *S-E* curves of the solid solution series at 2 Hz after pre-poling. **b**, Electric field dependent unipolar *S-E* curves of (PTMA)$CdBr_{2.7}Cl_{0.3}$ at 2 Hz. **c**, Contour plot of the large-signal d_{35}^* *versus* electric field and frequency. **d**, A comparison of shear piezoelectric coefficients of different ferroelectric materials (see **Supplementary Table S3** for references). Note that our sample shows a range of piezoelectric coefficients due to the electric field and frequency

dispersion. The values of Pb-based relaxors depend on composition and domain configuration. **e**, A comparison between the bipolar shear strain hysteresis loop of (PTMA)$CdCl_3$ and the typical butterfly longitudinal strain curve of PMN-PT in logarithm scale. **f**, A comparison between the unipolar shear strain responses of (PTMA)$CdBr_{2.7}Cl_{0.3}$ and PMN-PT. The slopes of the linear fits are the large signal piezoelectric coefficients.

Fig. 4 | Calculated switching barriers of (PTMA)$CdBr_3$ and (PTMA)$CdCl_3$. a, Minimum energy paths calculated using the generalized solid-state nudged elastic band (GSSNEB) method. **b**, Calculated integrated crystal orbital Hamilton populations (ICOHPs) of the Cd-X bond that breaks during switching (left), and the two shortest hydrogen bonds (middle and right).

Table 1| Structural information of (PTMA)$CdBr_{3x}Cl_{3(1-x)}$ in the LTP.

Br amount (%)	0	15	29	45	63	70	77	80	90
a / Å	12.7541	12.8262	12.8497	12.8960	12.9338	12.9763	12.9909	13.0015	13.0465
b / Å	14.5035	14.5961	14.6257	14.6785	14.7126	14.7458	14.7443	14.7601	14.7827
c / Å	7.1515	7.2275	7.2554	7.31681	7.3650	7.4153	7.4261	7.4567	7.5058
β / °	96.3069	95.910	95.823	95.5064	95.282	94.985	95.035	95.000	94.841
Vol / $Å^3$	1314.86	1345.89	1356.50	1378.63	1395.54	1413.54	1416.92	1425.52	1442.43
Space Group	*Cc*	*Cc*	*Cc*	*Cc*	*Cc*	*Cc*	*Cc*	*Cc*	*Cc*

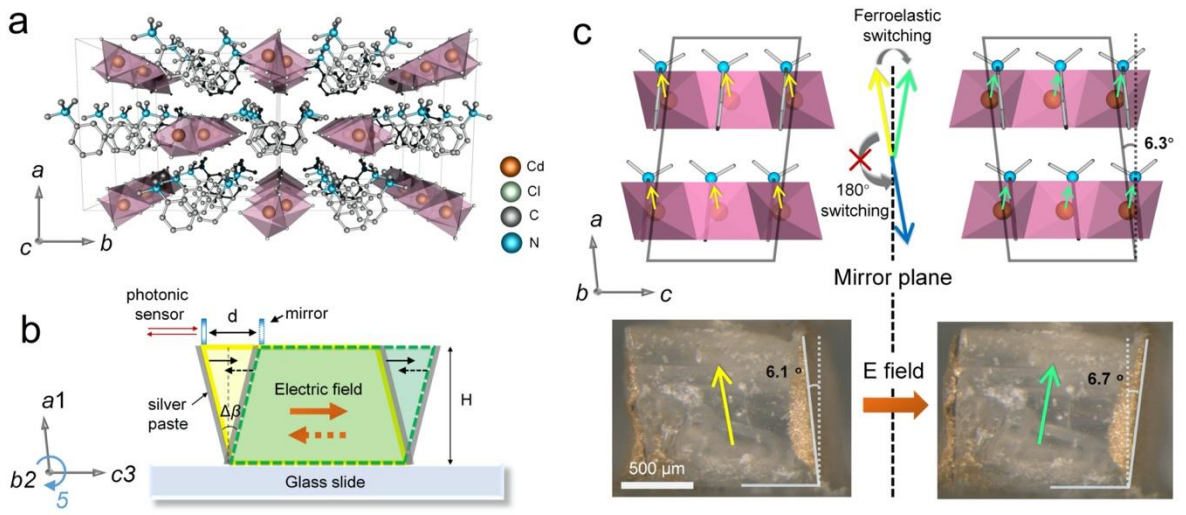

Fig. 1 | Crystal structures and photos of (PTMA)$CdCl_3$ in two different ferroelastic states. **a**, Perspective of crystallographic structure along the 1D chain (*c*) direction. **b**, Experimental setup for the shear strain and piezoelectricity measurements. Silver paste is applied on the *ab* planes of the crystal as electrodes, and the electric field is applied along the 1D chain (*c*) direction. The numbers in the coordinate denote the Voigt notation of the strain tensor. **c**, Upper panel: Illustration of structural units in the two ferroelastic states and structure confinement effect for ferroelectric/ferroelastic switching. Yellow and green arrows indicate polarization directions. Lower panel: Photos of a bulk single crystal poled to the two ferroelastic states by electric field, showing a macroscopic shear strain in good correlation with the unit cell distortion.

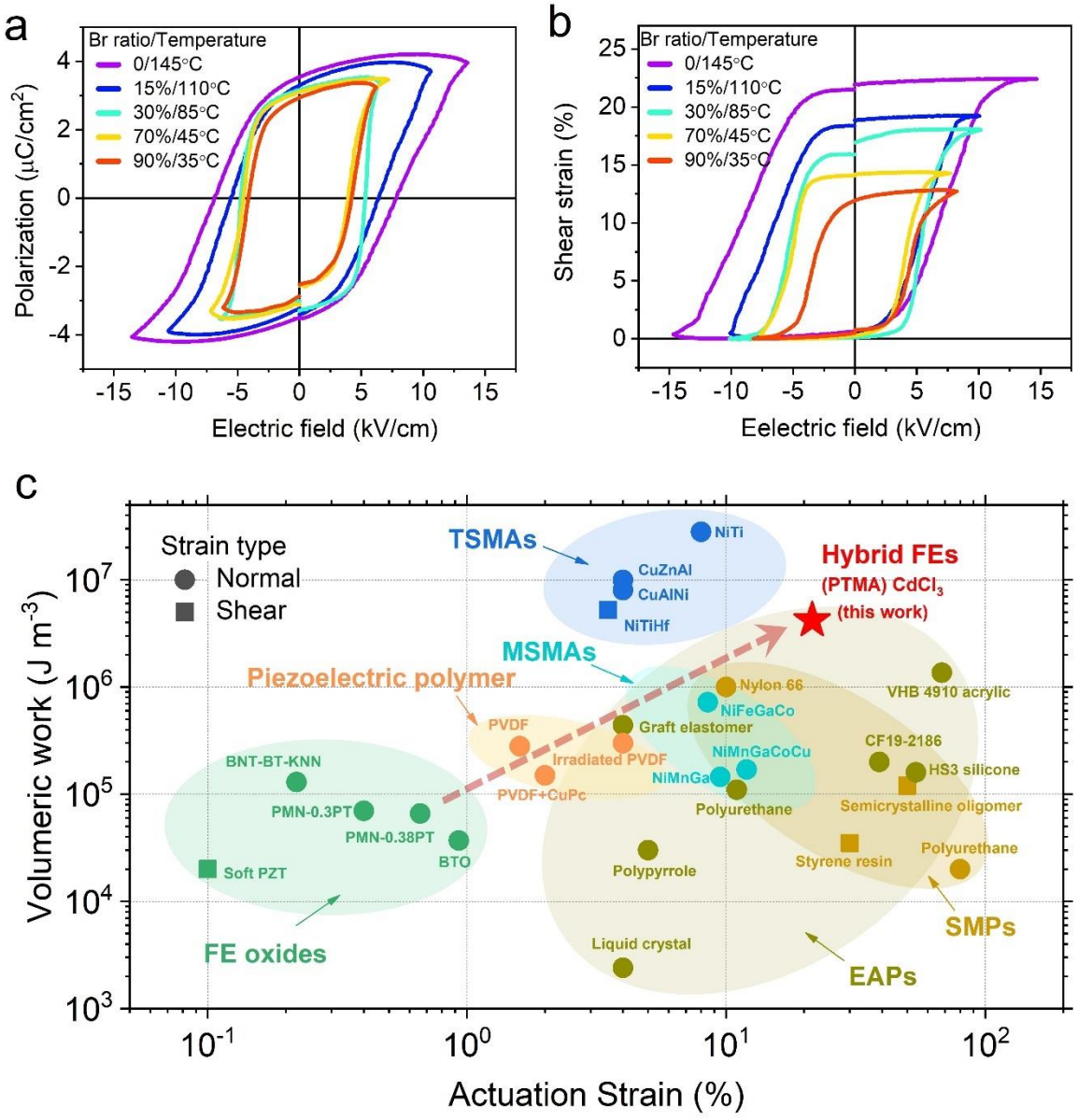

Fig. 2 | Ferroelectric and ferroelastic properties of (PTMA)$CdBr_{3x}Cl_{3(1-x)}$. a, *P-E* loops and **b**, shear *S-E* loops of the solid solution series at a measurement frequency of 2 Hz. **c**, Actuation strain and work outputs for various material systems, i.e., ferroelectric (FE) oxides, piezoelectric polymer, magnetic-driven shape memory alloys (MSMAs), temperature-driven shape memory alloys (TSMAs), electroactive polymers (EAPs), shape memory polymers (SMPs) and hybrid FE (see **Supplementary Table 2** for detailed data and references).

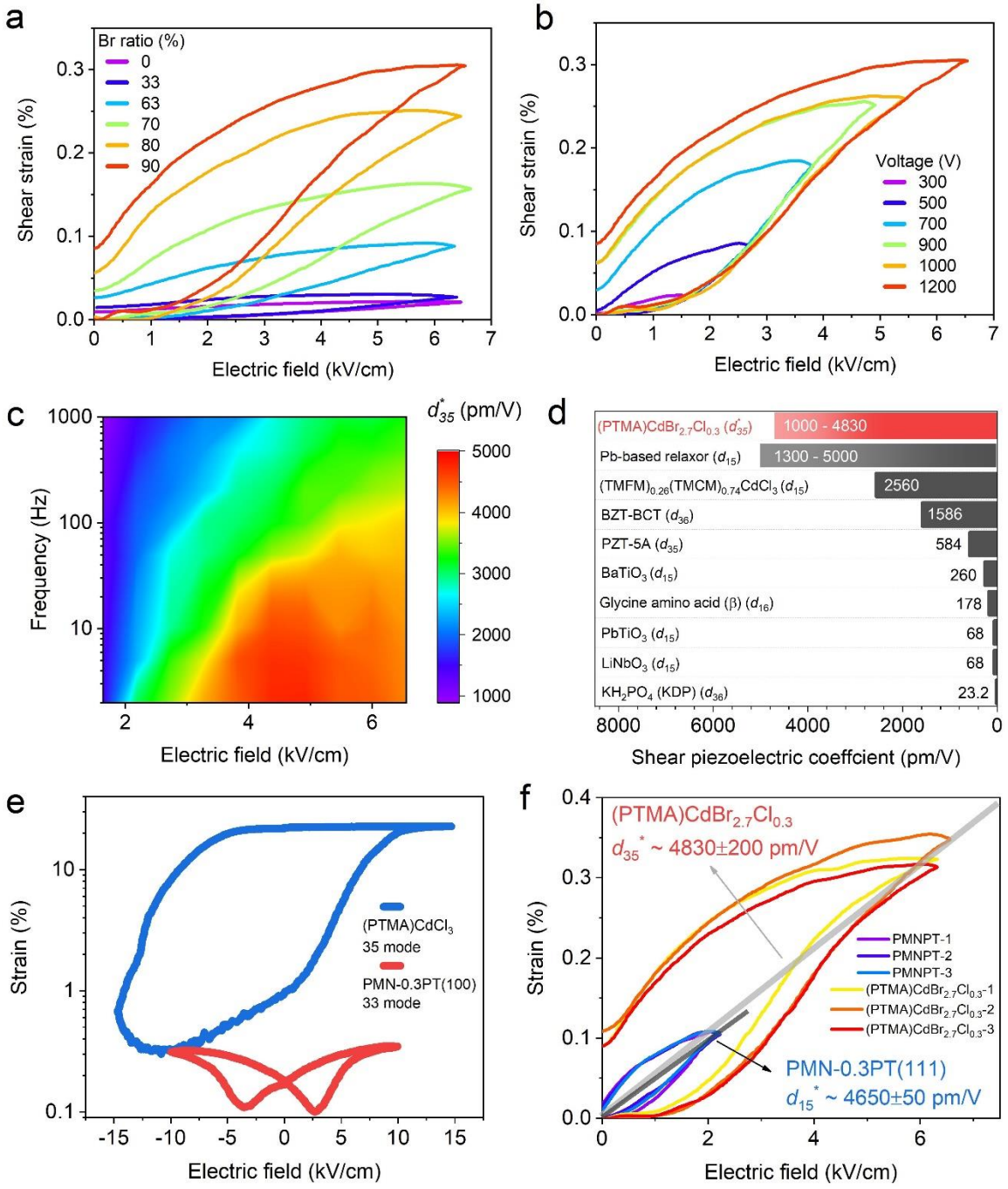

Fig. 3 | Large-signal piezoelectric properties of (PTMA)CdBr$_{3x}$Cl$_{3(1-x)}$. **a**, Unipolar *S-E* curves of the solid solution series at 2 Hz after pre-poling. **b**, Electric field dependent unipolar *S-E* curves of (PTMA)CdBr$_{2.7}$Cl$_{0.3}$ at 2 Hz. **c**, Contour plot of the large-signal d^*_{35} *versus* electric field and frequency. **d**, A comparison of shear piezoelectric coefficients of different ferroelectric materials (see **Supplementary Table S3** for references). Note that our sample shows a range of piezoelectric coefficients due to the electric field and frequency dispersion. The values of Pb-based relaxors depend on composition and domain configuration. **e**, A

comparison between the bipolar shear strain hysteresis loop of (PTMA)$CdCl_3$ and the typical butterfly longitudinal strain curve of PMN-PT in logarithm scale. **f**, A comparison between the unipolar shear strain responses of (PTMA)$CdBr_{2.7}Cl_{0.3}$ and PMN-PT. The slopes of the linear fits are the large signal piezoelectric coefficients.

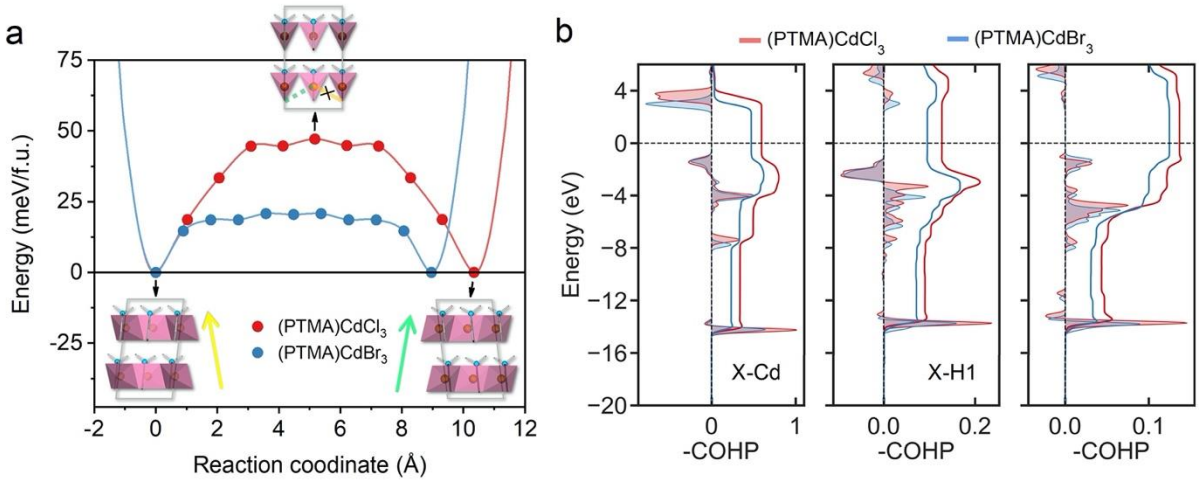

Fig. 4 | Calculated switching barriers of (PTMA)CdBr$_3$ and (PTMA)CdCl$_3$. a, Minimum energy paths calculated using the generalized solid-state nudged elastic band (GSSNEB) method. **b**, Calculated integrated crystal orbital Hamilton populations (ICOHPs) of the Cd-X bond that breaks during switching (left), and the two shortest hydrogen bonds (middle and right).